




Electrochemical detection of dopamine using van der waals-interacted NiO–ZnO-functionalized reduced graphene oxide nanocomposite

Ganesh K. Chougule¹, Anita K. Tawade², Jayashri V. Kamble³, Kiran Kumar K. Sharma², Sawanta S. Mali⁴, Chang Kook Hong⁴, Anil A. Powar⁵, Kishor V. Gaikwad^{1,*}, and Shivaji N. Tayade^{3,*} 

¹ Department of chemistry, Rajarshi Chhatrapati Shahu College, Kolhapur, Maharashtra 416004, India

² School of Nanoscience and technology, Shivaji University, Kolhapur, Maharashtra 416004, India

³ Department of Chemistry, Shivaji University, Kolhapur, Maharashtra 416004, India

⁴ Department of Advanced Chemical Engineering, Chonnam National University, Gwangju 61186, South Korea

⁵ Department of Chemistry, Walchand College of Engineering, Sangli, Maharashtra 416415, India

Received: 20 August 2023

Accepted: 4 January 2024

© The Author(s), under exclusive licence to Springer Science+Business Media, LLC, part of Springer Nature, 2024

ABSTRACT

The in situ Nickel oxide-zinc oxide-doped reduced graphene oxide (NiO–ZnO/rGO) nanocomposite is synthesized by the hydrothermal method. NiO–ZnO/rGO nanocomposite-modified glassy carbon electrode (GCE) utilized as electrochemical sensor for dopamine sensing. Scanning electron microscopy (SEM), RAMAN spectroscopy, Transmission electron microscopy (TEM), X-ray diffraction (XRD), and X-ray photoelectron spectroscopy (XPS) were used for morphological and structural characterizations of NiO–ZnO/rGO nanocomposite. Further investigation of the redox response and the charge transfer characteristics of dopamine (DA) at NiO–ZnO/rGO-modified GCE tested using cyclic voltammetry and electrochemical impedance spectroscopy. The prepared GCE nanocomposite-modified electrochemical sensor show a linear response of redox peak current for DA in the concentration range of 0.0041–0.054 μM . The active electrochemical surface area of the sensor found to be $2.1 \times 10^{-6} \text{ cm}^2$, with low detection limit of 0.0076 μM and high sensitivity of $12.19 \mu\text{A L cm}^{-2} \text{ Mol}^{-1}$. The constructed sensor has close to 100% recovery toward DA in voluntarily collected human urine samples. The composite exhibits good reproducibility for sensing DA for month, which is an indication of their repeatability. Also designed sensors show 123% retention current to 100 cycles of CV indicates the good stability of the sensor to DA, which are crucial for the fabrication of further devices.

Address correspondence to E-mail: kishuvgaikwad@rediffmail.com; snt_chem@unishivaji.ac.in

1 Introduction

An important factor that influences the sensitivity of nanosystem-designed sensors to biomarkers in electrochemical sensing is Van der Waals-type interactions. Due to the delocalized sp^2 carbon domains, it is well known that n-type carbonaceous materials, such as reduced graphene oxide, are strongly conductive along the basal plane [1]. This domain of the basal plane is a center for nanomaterials to reserve their position through a unique Van der Waals interaction. These interactions alter the electronic properties of a material by deforming its planar band structure. This deformation of the band structure of the composite materials mimics the redox energy of the analyte under observation, resulting in an effective charge transfer process between the composite and the analyte [2].

Dopamine (3, 4-dihydroxyphenylethylamine, DAH₂), an important catecholamine neurotransmitter, is present in mammalian brain tissue [3]. It functions as an extracellular molecular messenger in the central nervous, renal, endocrine and cardiovascular systems. Neurological conditions such as Parkinson's disease, schizophrenia, convulsions, dementia in the elderly, and hyperactivity disorder (HDD) can develop when the dopamine system in the body malfunctions or becomes abnormally concentrated [4]. For such real-time diagnosis and continuous monitoring of dopamine, a quantitative technique must be devised in order to accurately identify and estimate dopamine levels.

To design and produce a low-cost biomarker, researchers have focused a significant portion of their efforts on developing biomarker-sensing materials that are both stable and highly sensitive. Numerous diseases, including diabetes, cancer, and abnormalities in neurotransmitters, can be detected in their earliest stages using concentration-dependent electron transport between a modified composite electrode and the analyte [5]. Numerous synthesis techniques, including hydrothermal, microwave, chemical solution, and the sol-gel process, are employed in the fabrication and synthesis of new materials [6]. Hydrothermal techniques include those that synthesize metal oxides at high temperatures and pressures with minimal chemical residue and high-quality products.

For the detection of dopamine, numerous analytical techniques are available, including High-performance liquid Chromatography (HPLC), Ultraviolet (UV)

spectroscopy, flow injection analysis, fluorescence, and electrochemical detection [7, 8]. Electrochemical techniques have been validated for their speed, simplicity, and compactness; electrochemical detection stands out among them. Due to two-dimensional (2D) structure, high sensitivity, component shape, and enormous active surface area graphene oxide, Chalcogenide [9], and its associated composites have proven to be an effective draw for potential applications, such as biosensing [10].

In recent years, techniques including sol-gel [11], reverse micelle, electrodeposition, microwave irradiation, and laser-induced fragmentation have been utilized to produce graphene oxide, nickel oxide, and zinc oxide nanoparticles. The hydrothermal synthesis of NiO-ZnO/rGO has proven to be an efficient, one-spot [12], cost-effective, and easy method due to its simplicity and favorable reaction conditions [13]. The electrocatalytic behavior of dopamine on NiO-ZnO NPs decorated on rGO nanocomposites has been investigated using glassy carbon electrodes. GO modified and NiO-ZnO-modified electrodes have also been subjected to comparative investigations. All detection processes employ physiological pH conditions. Using electrochemical methods, it is possible to estimate the limits of quantification (LOQ), the limits of detection (LOD), and the interference of other biomolecules, such as Hydrogen Peroxide [14], ascorbic acid [15], uric acid [16], and glucose [17].

In the past decade, different types of materials have been used for dopamine sensing. With excellent sensitivity (1.45 $\mu\text{A}/\mu\text{M}$), dopamine has been investigated using Fe₃O₄ and ZnO nanoparticles doped with phthalocyanine (Pc) and functionalized MWCNTs [18]. A new electrochemical sensor with a limit of detection of 0.04 μM for the measurement of dopamine based on flower-shaped zinc oxide (ZnO) nanoparticles has been revealed [19]. For the quantitative analysis of dopamine as well as the assay of dopamine in various real samples, it has been shown that the GCE/MWCNT/NiO demonstrated strong linear characteristics in the concentration range from 4×10^{-5} μM to 6.25 μM [20]. A powerful electroactive catalyst for the detection of dopamine (DA) has been developed in this study using the hydrothermal method. This 2, 6 diaminopyridine functionalized electrochemically reduced graphene oxide with molybdenum oxide ternary composites (2, 6 DAP-ERGO/MoO₃) [21]. For the first time, dopamine (DA), acetaminophen (AP), and melatonin

(MEL) were simultaneously sensed using the glassy carbon electrode surface, which was modified with undoped α - Fe_2O_3 , platinum-doped Fe_2O_3 (dPt Fe_2O_3), Pt-decorated Fe_2O_3 (sPt Fe_2O_3), and doped and decorated Fe_2O_3 (sdPtFe) [22]. When designing a DA sensor, graphene-based materials and their distinctive electrical characteristics make excellent sensing materials [23]. With an effective 14.5% response, a new microwave-assisted two-dimensional (2D) hybrid material based on nanostructured reduced graphene oxide (rGO) doped with Pd nanoparticles (Pd/rGO) has been constructed to study hydrogen sensing [24]. The rGO- WS_2 @ Fe_3O_4 nanocomposite exhibited a low limit of detection (LOD) of 2.74 μM and a sensitivity of 3.18 $\mu\text{A } \mu\text{M}^{-1} \text{ cm}^{-2}$ for dopamine [25].

In the present study, we have explored the synthesis of NiO–ZnO/rGO nanocomposite using the hydrothermal method for selective detection of DA in acetate buffer media (pH 7.4). This nanocomposite has a morphology different from that of other studies and NiO–ZnO/rGO with a hexagonal shape and rods adhered and merged in an rGO sheet. This unique structure provides the Van der Waals interaction force. The results were obtained, which overcome limitations regarding the limits of detection and sensitivity. This electrochemical sensing characteristics such as sensitivity, linear range, limit of detection and quantification, repeatability, and stability of DA in different pH media are investigated to explore the low-cost characteristics of NiO–ZnO/rGO nanocomposite-modified electrodes.

Novelty of this work:

- Van der Waals interaction of the hexagonal shape of ZnO and the rods of NiO on a reduced graphene oxide sheet.
- NiO–ZnO/rGO nanocomposite for dopamine sensing has first time reported.
- Hydrothermal method is simple, cost-effective, efficient, and favorable in all reaction conditions.
- Observed Limit of Detection is extremely low (0.0076 μM).

2 Experimental techniques

2.1 Reagents

Graphite flakes (mesh size 100 μm), Sulfuric acid (99% AR), Phosphoric acid (AR 88%), Potassium permanganate (KMnO_4) (AR), Dimethyl Sulfoxide

(DMSO) (99% AR), hydrochloric acid (98% AR), hydrogen peroxide (H_2O_2), ethyl alcohol (99% AR), diethyl ether (AR), Zinc nitrate Hexahydrate (AR), Nickel nitrate Hexahydrate (AR), and Ethylene glycol (AR) were purchased from Sigma-Aldrich. Dopamine (DA) was purchased from Fluka Chemical Co. (USA) and used without further purification. The 0.1-M pH 7.4 acetate buffer was prepared by employing a sodium acetate and acetic acid solution (CH_3COOH and CH_3COONa from Merck; 0.1-M total acetate), which was the supporting electrolyte used in all studies.

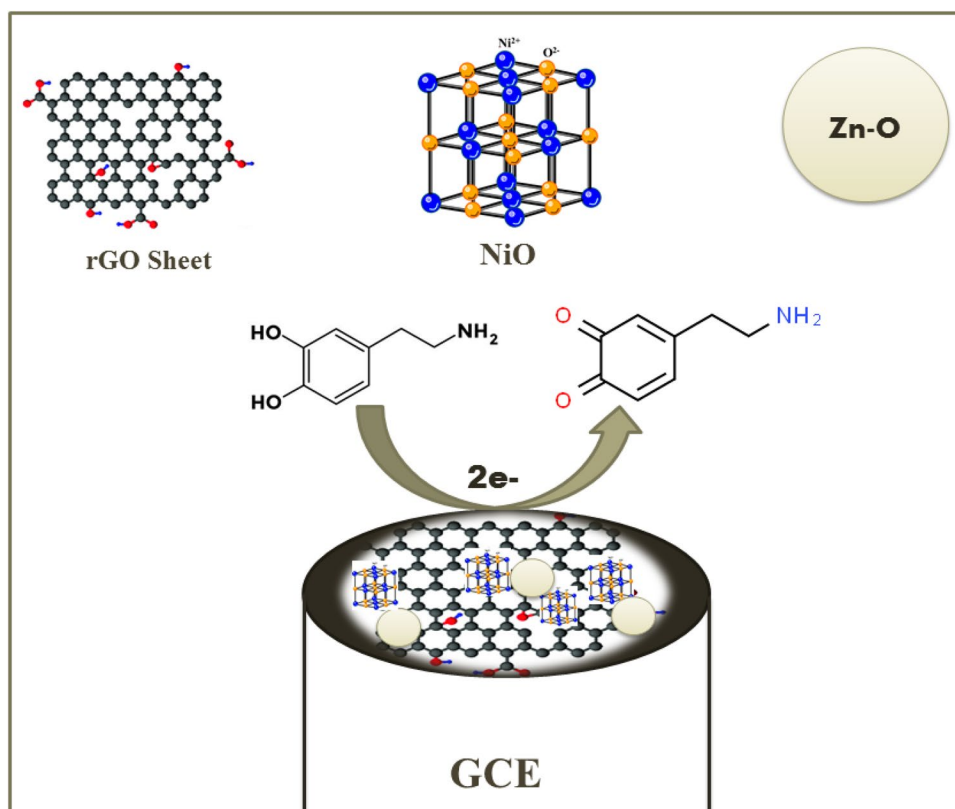
2.2 Preparation of NiO–ZnO nanoparticles

1.485 g of Zinc nitrate Hexahydrate [$\text{Zn}(\text{NO}_3)_2 \cdot 6\text{H}_2\text{O}$], 1.455 g of Nickel nitrate Hexahydrate [$\text{Ni}(\text{NO}_3)_2 \cdot 6\text{H}_2\text{O}$], and 1.6 g of Sodium hydroxide were added to 50 ml of ethanol (99%) and stirred for 10 min at ambient temperature. 2 ml of Ethylene glycol were thoroughly added to the reaction mixture. The entire reaction mixture was transferred to spotless Teflon, sealed in an autoclave, and then heated at 180 $^\circ\text{C}$ in muffle furnace for 24 h. After cooling to ambient temperature, the resultant material was centrifuged and rinsed with ethanol and twice with double distilled water. NiO–ZnO nanoparticles (Creamish in color) are dried at 120 $^\circ\text{C}$ in hot-air oven.

2.3 Preparation of NiO–ZnO/rGO nanocomposite

Graphene oxide (brown in color) was synthesized using an improved Hummers method [26]. Dried GO was dispersed in 10 mL of double distilled water. To prepare NiO–ZnO/rGO composite in a typical experiment, 1.485 g of Zinc nitrate Hexahydrate [$\text{Zn}(\text{NO}_3)_2 \cdot 6\text{H}_2\text{O}$], 1.455 g of Nickel nitrate hexahydrate [$\text{Ni}(\text{NO}_3)_2 \cdot 6\text{H}_2\text{O}$], and 1.6 g of sodium hydroxide in 50 ml of ethanol (99%) were added, stir for 10 min at ambient temperature, and finally add 6 ml of aqueous GO solution and then stir for 10 min. After adding 2 mL of Ethylene glycol, the mixture must be thoroughly blended. The entire reaction mixture was transferred to spotless Teflon, sealed in an autoclave, and heated at 180 $^\circ\text{C}$ in muffle furnace for 24 h. After cooling to ambient temperature, the resultant material was centrifuged and rinsed with ethanol and twice with double distilled water. The NiO–ZnO/rGO (Pale green in color) composite is dried at 120 $^\circ\text{C}$ in hot-air oven.

Mechanism of this work.



2.4 Preparation of NiO-ZnO/rGO composite-modified GCE

The NiO-ZnO/rGO composite (1 mg/ml in ethanol) was deposited on glassy carbon electrode (GCE) by a drop and dry method at room temperature. The electrode was further allowed to dry in the ultra-high pure nitrogen atmosphere for about 30 min. The loosely bound composite was removed by a gentle cleaning of modified GCE with double distilled water. NiO-ZnO nanoparticles (NPs)-modified GCE, ZnO-modified GCE, and GO NPs-modified GCE were also prepared for comparative study with the NiO-ZnO/rGO composite.

2.5 Instrumentation

Using the electrochemical workstation PGSTAT 302 N (Metrohm Autolab), a standard three-electrode cell with a platinum wire as the counter electrode, Ag/AgCl/saturated KCl as the reference electrode, and bare or NiO-ZnO nanoparticle-modified GCE (geometric area = 0.07 cm²) as the active electrode.

The GCE was polished using alumina powder of 25 μm sizes and washed sequentially three times with ethanol and water to remove all traces of alumina and impurities. A thermal analyzer from TA Instruments, the SDT Q600, was used for the thermogravimetric analysis-differential scanning calorimetry (TGA-DSC) analysis. Using a spinning anode X-ray source and a Bruker D8 Advance X-ray diffractometer (XRD) operating at Cu-K monochromatic radiation (= 1.5418 Å), the phase characterization of nanocomposites was carried out. Thermo Scientific XPS (VG Multilab 2000-Thermo Scientific, USA, K-Alpha), which can withstand high photonic energies of 0.1 to 3 keV, was used to collect the X-ray photoelectron spectra (XPS). For Raman analysis Renishaw INVIA 0120-02 (UK) Raman spectrometer was used. Thermo Scientific's K-alpha + spectrometer was used for High-resolution Transmission electron microscope (HRTEM). Hitachi SU-70 (Japan) was used to carry out the field emission scanning electron microscope (FE-SEM) measurement. All electrochemical tests were performed at a temperature of 25 ± 1 °C in a 0.1-M acetate solution with a pH of 7.4.

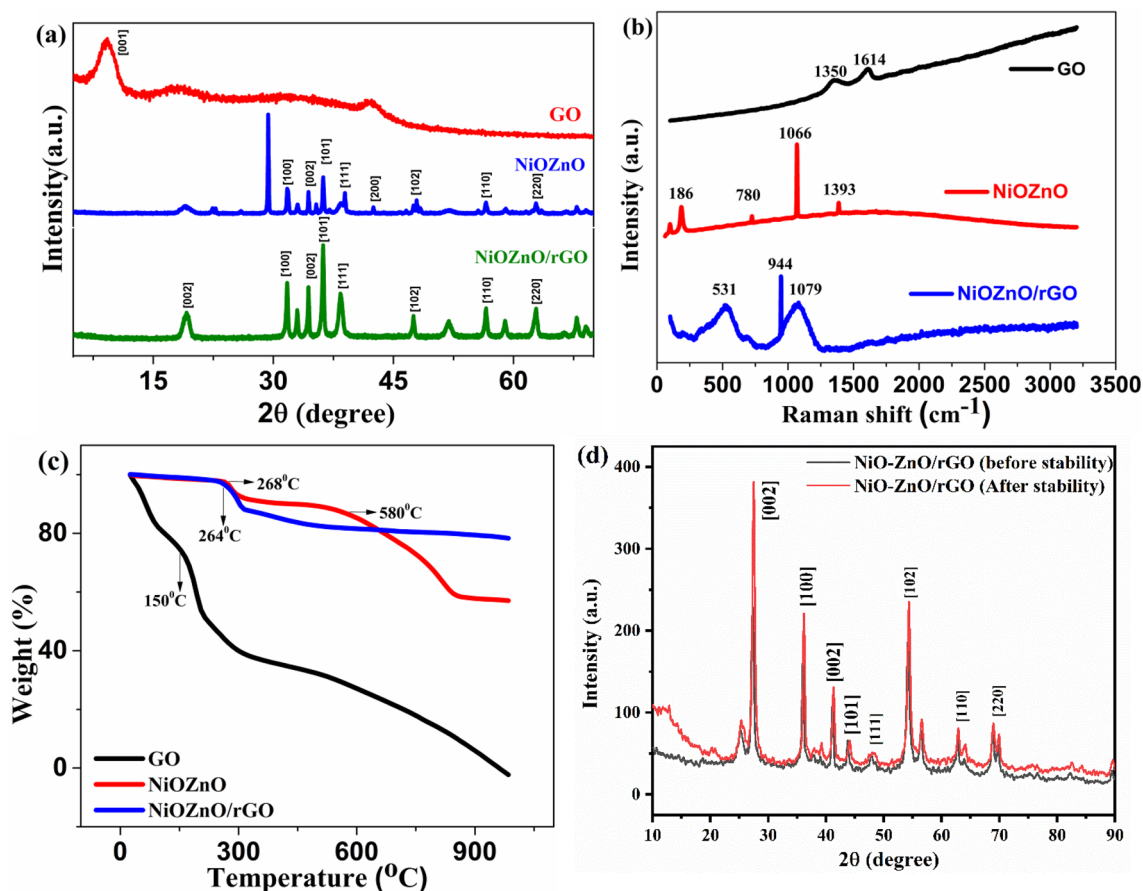


Fig. 1 **a** XRD pattern of GO, NiO–ZnO, and NiO–ZnO/rGO composite. **b** Raman spectra of GO, NiO–ZnO, and NiO–ZnO/rGO. **c** TGA curves of GO, NiO–ZnO, and NiO–ZnO/rGO. **d** XRD overlay of NiO–ZnO/rGO before and after stability

3 Results and discussion

3.1 X-ray diffraction study of NiO–ZnO/rGO composite

The XRD measurement was conducted in 2θ range from 5° to 80° at the scan rate of $0.1^\circ/\text{min}$. Figure 1a of the XRD pattern depicts the precise diffraction point at 9.20° , which reveals the pure (001) plane of Graphene oxide (GO), as reported in the literature [27]. The distance between planes can be calculated using Bragg's equation [28]:

$$n\lambda = 2d \sin \theta. \quad (1)$$

Bragg's equation is used to calculate d-spacing in GO and NiO–ZnO/rGO composite. In GO, d-spacing is 0.06 nm. The samples confirm Orthorhombic NiO–ZnO/rGO phase crystalline structure (JCPDS No. 47-1019) [29]. The interlayer spacing of rGO is

~ 0.13 nm at 36.26° (111) in composite. The value of spacing is nearly three times smaller as compared to reported [30], [31] values for rGO that indicates specific and defined intercalation of NiO–ZnO. The calculated spacing for rGO is greater than GO that indicates further confirmation of the intercalation of NiO–ZnO in successive rGO sheet. The NiO–ZnO/rGO composite's increased layer-to-layer spacing indicates that the NiO–ZnO NPs are well decorated on the rGO sheet.

Figure 1d represents XRD overlay of NiO–ZnO/rGO before and after stability. It is observed that XRD peak position are constant. However, we found that XRD spectra of composite shows slightly increase in intensity peak [32]. This is attributed to catalytic behavior appearing from all the planes of nanocomposite and due to this, 123% retention current takes place which is shown in Fig. 7b.

3.2 Raman spectra of NiO–ZnO/rGO composite

Crystal structure, disorder, and defects in carbon-based materials are typically summarized by Raman spectroscopy. GO indicates the G band at 1614 cm^{-1} and the D band at 1350 cm^{-1} , as shown in Fig. 1b. The G band in GO is associated with the stretching motion of symmetric sp^2 bonds of carbon atoms, while the D band ascribes disorder and local defects indicating sp^3 bonds of structure [33]. The Raman spectra of the NiO–ZnO/rGO composite show a characteristic peak at 944 cm^{-1} and 1079 cm^{-1} [34]. This is 1079 cm^{-1} due to the overlapping of NiO and ZnO peaks. The change in peak location shows that during hydrothermal processes, GO was reduced to rGO [35]. In addition, this peak revealed the presence of weak interaction between NiO–ZnO and a graphene oxide sheet as a Van der Waals force, which affects the vibrational and electronic states of the composite [36]. In addition, one additional peak arises at 531 cm^{-1} indicating lattice vibration of NiO.

3.3 Thermogravimetric investigations of NiO–ZnO/rGO composite

Figure 1c depicts a typical NiO–ZnO/rGO composite TGA curve at a heating rate of $10\text{ }^\circ\text{C}/\text{min}$. The TGA profile reveals a decrease in mass with a nearly abrupt change at $264\text{ }^\circ\text{C}$ with 9.3% weight loss, followed by a constant plateau. Therefore, above $300\text{ }^\circ\text{C}$, a stable composite material appears to form. Similarly, the TGA curve of NiO–ZnO NPs demonstrates two relatively abrupt changes at 268 and $580\text{ }^\circ\text{C}$. At $150\text{ }^\circ\text{C}$, the TGA curve for GO NPs displays a quasi-sharp change.

3.4 XPS spectra of NiO–ZnO/rGO NPs

To examine the entire chemical structure of the as-prepared NiO–ZnO/rGO composite, X-ray photoelectron spectroscopy (XPS) was used. Figure 2a presents the C 1s spectra of the composite, in which the peaks appearing at 284.06 eV (C=C bond), 284.8 eV (C–C bond), 286.9 eV (C–O bond), and 288.3 eV (O–C–O/C=O bond) coincided with sp^2 carbon components [37]. Figure 2e depicts the C 1s spectrum of GO and the shifting of the whole C 1s spectrum toward higher binding energy (blue shift) in GO as

compared to the C 1s spectra of the NiO–ZnO rGO composite, attributed to the conversion of GO into rGO. It is possible that the highly conductive rGO in the composite could serve as a conductive network to increase the number of electron transfer paths within the material and cause Van der Waals forces of attraction with NiO–ZnO. From the Electrochemical Impedance Spectroscopy (EIS) study, the lower values of charge transfer resistance R_{ct} possibly confirm favorable electron transport between DA and NiO–ZnO/rGO-modified electrodes.

Figure 2b shows O 1s XPS peaks, the band at 529.0 and 530.0 eV can be indexed to the C=O bond; the band at 531.0 eV can be indexed to lattice oxygen (OL) in the hexagonal ZnO's wurtzite structure [38]. The $2p_{3/2}$ main peak at 854 eV and its satellite at 860 eV , as well as the $2p_{1/2}$ main peak at 872 eV and its satellite at 878 eV , in the Ni 2p spectrum in Fig. 2c, exhibit the presence of NiO [39]. Figure 2d shows the Zn 2p spectrum, with two bands at 1043.0 and 1020.0 eV , corresponding to Zn $2p_{1/2}$ and Zn $2p_{3/2}$ in the form of ZnO, respectively. From the overall XPS analysis of the composite materials, we confirm the formation of NiO–ZnO/rGO nanocomposite materials.

3.5 Morphological and structural analysis

The morphology and structure of the as obtained GO, NiO–ZnO, and NiO–ZnO/rGO composite materials were analyzed using field emission scanning electron microscopy (FE-SEM) and transmission electron microscopy (TEM). Figure 3a depicts the pattern of graphene oxide with the oxygenated planar sheet in two dimensions. Figure 3b depicts the image of NiO–ZnO, which is embedded with 200 nm -sized hexagonal ZnO and peanut-shaped NiO rods [40]. Figure 3c illustrates NiO–ZnO/rGO with a hexagonal shape and rods adhered and merged in a 200-nm rGO sheet. This unique structure provides the Van der Waals interaction force, which has an effect on the extremely low dopamine detection limit. As well as crystalline GO, NiO–ZnO, and NiO–ZnO/rGO, as shown in Fig. 3d–f by SAED patterns at a thickness of 30 nm .

Figure 4c shows SEM images of NiO–ZnO, further confirming that the whole surface of NiO is uniformly coated with a large amount of ZnO nanoparticles which further adhered and merged into rGO sheet. The nanoplatform of rGO is diminished by the loading of NiO and ZnO, and this leads to their random dispersion throughout the rGO [41]. Figure 4a and b

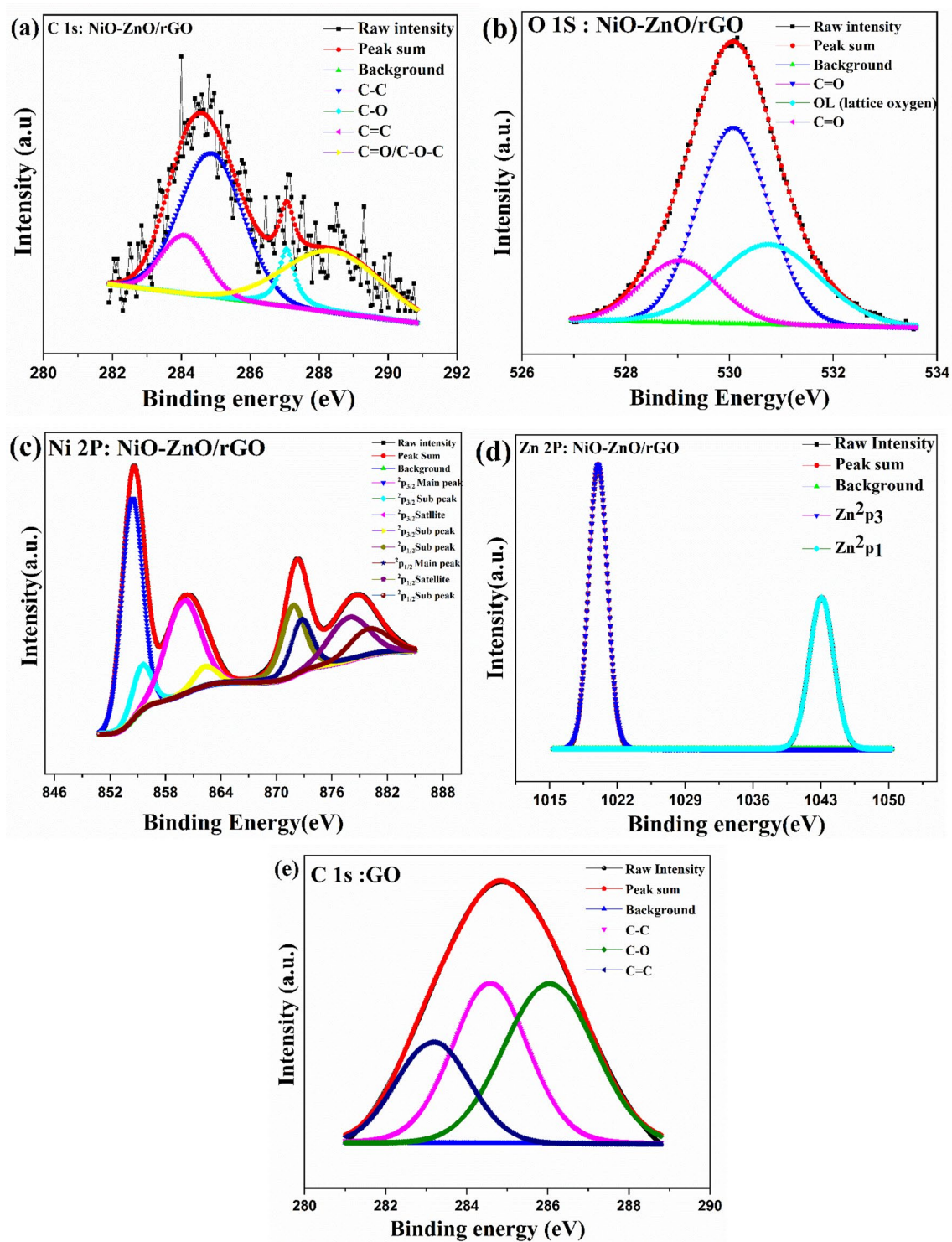


Fig. 2 XPS spectra of NiO-ZnO/rGO composite: **a** C 1s, **b** O 1s, **c** Ni 2p, **d** Zn 2p, XPS spectra of GO: **e** C 1

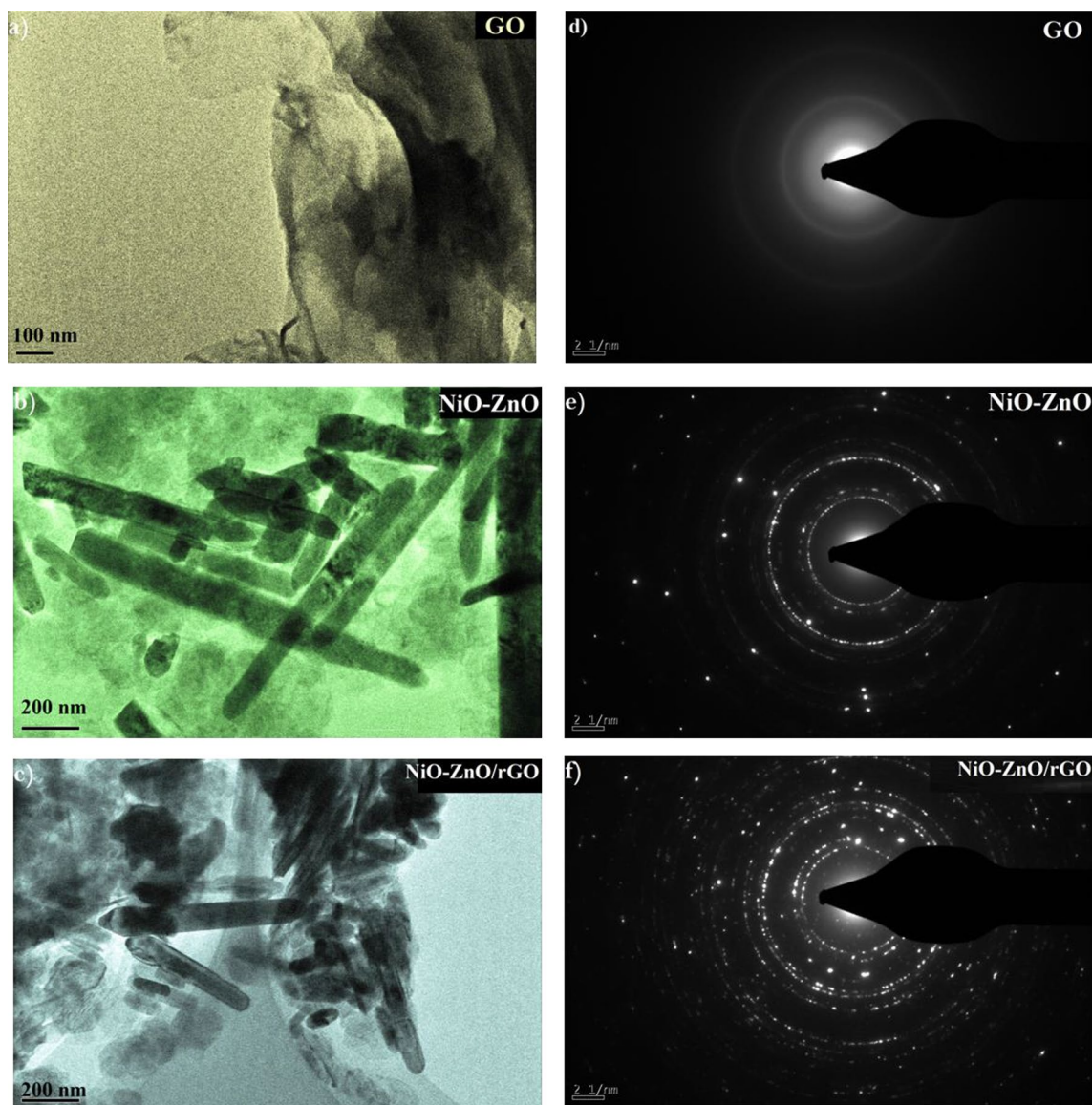


Fig. 3 TEM image of **a** GO; **b** NiO–ZnO, and **c** NiO–ZnO/rGO composite, SAED pattern images at 30 mm of **d** GO; **e** NiO–ZnO, and **f** NiO–ZnO/rGO composite

shows graphene oxide sheet and mixed structure of rods and hexagonal shape of NiO and ZnO with high resolution at 500 nm, respectively.

Comparative elemental analysis between GO, NiO–ZnO, and NiO–ZnO/rGO, as shown in Table 1 and in Fig. 4d. Elemental Detection Spectra (EDS) of the NiO–ZnO/rGO composite demonstrate that oxygen depletion in the nanocomposite due to removal of insulating oxygen groups. Better electronic conductivity results from allowing electrons to delocalize. Therefore, it enhances its electrical conductivity.

3.6 The electrochemical behavior of NiO–ZnO/rGO-modified electrode

Figure 5a depicts blank CVs (without DA) at the GCE modified by NiO–ZnO/rGO, NiO–ZnO, and GO in 0.1-M acetate buffer (pH 7.4). In blank CVs, no characteristic signature of faradic activity observed confirms the electrode system is stable, noise less, and buffer is free of redox active impurities in the preferred electrochemical window. Figure 5b represents the overlay CVs of increasing concentrations of DA in the range of 4.12–53.6 nM at 50 mV/s. The increase

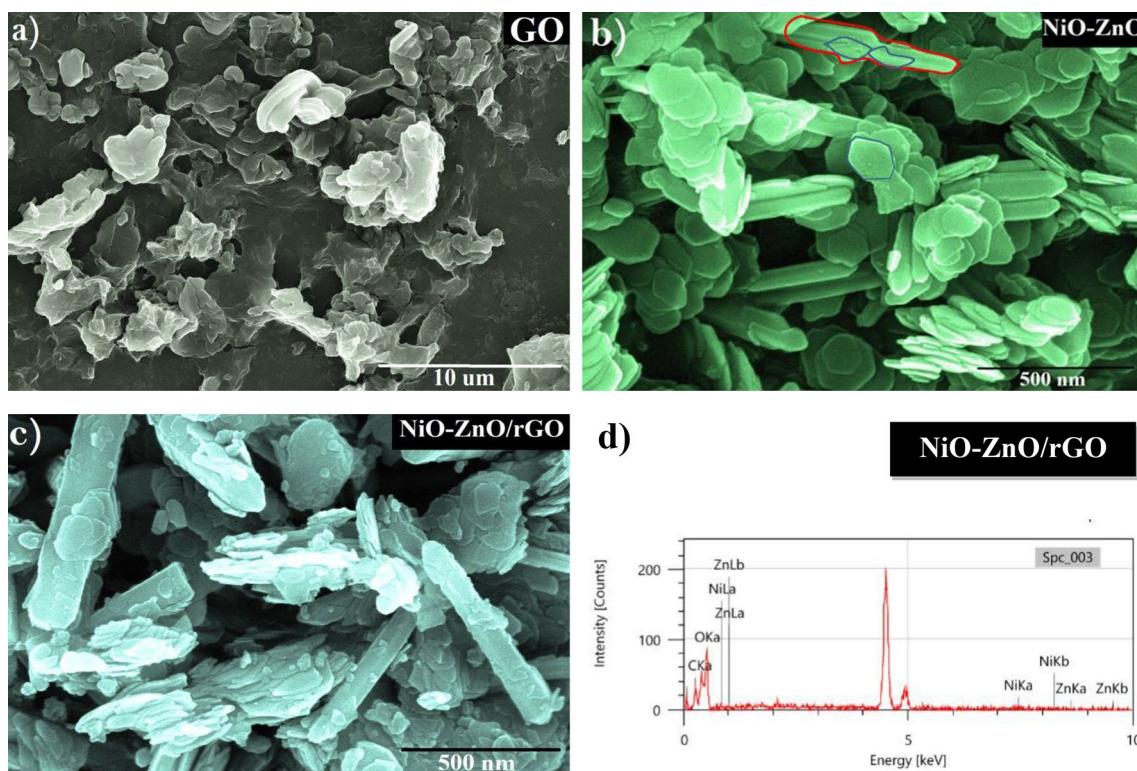


Fig. 4 SEM image of **a** GO, **b** NiO–ZnO (red-marked NiO rods and blue-marked Hexagonal shape of ZnO), and **c** NiO–ZnO/rGO composite. **d** Elemental detection spectra of NiO–ZnO/rGO nanocomposite

Table 1 Elemental analysis (EDS) of GO, NiO–ZnO, and NiO–ZnO/rGO

Sample	C (at%)	O (at%)	Ni (at%)	Zn (at%)
GO	60.48%	39.12%	–	–
NiO–ZnO	–	65.65%	17.90%	16.45%
NiO–ZnO/rGO	42.91%	56.12%	0.89%	0.08%

in concentration of DA shows no appreciable change in the peak potential shifting, which confirms the oxidized products of DA are not accumulating at the surface of the electrode. It is also observed that the oxidation peak current increases upon increasing the DA concentration. The linear response of peak current with concentration of DA is depicted in Fig. 5c. This special characteristic of linearity is ascribed to the diffusion-controlled oxidation of DA at the composite surface. This linear calibration graph of anodic pulse peak current (I_{pa}) versus rising DA concentration shows a linear correlation equation. Thus, the modified NiO–ZnO/rGO electrode can be effectively used for the determination of DA and for the future DA oxidation.

NiO–ZnO/rGO-modified GCE was further tested for potential pumping effects per second (scan rate). The effect of the scan rate on the electrochemical oxidation of DA was examined at different scan rates in the range of 10–100 mVs^{-1} as shown in Fig. 5d. The potential pumped per second (scan rate) studies were carried out to determine the nature of the electron transfer process dependency on the diffusion of the analyte, as shown in Fig. 5e. Thus, we found the linear correlation coefficient of 0.98 between the obtained peak current with scan rates that confirms that DA oxidation and reduction are quasi-reversible diffusion-controlled processes. This finding indicated that the modified electrode was subject to a diffusion-controlled process. The equation for anodic peak current and cathodic peak current with correlation coefficient is as follows:

Anodic peak current equation:

$$y = 1.16175 \times 10^{-7} + 1.16175 \times 10^{-6}(R^2 = 0.9841). \tag{2}$$

Cathodic peak current equation:

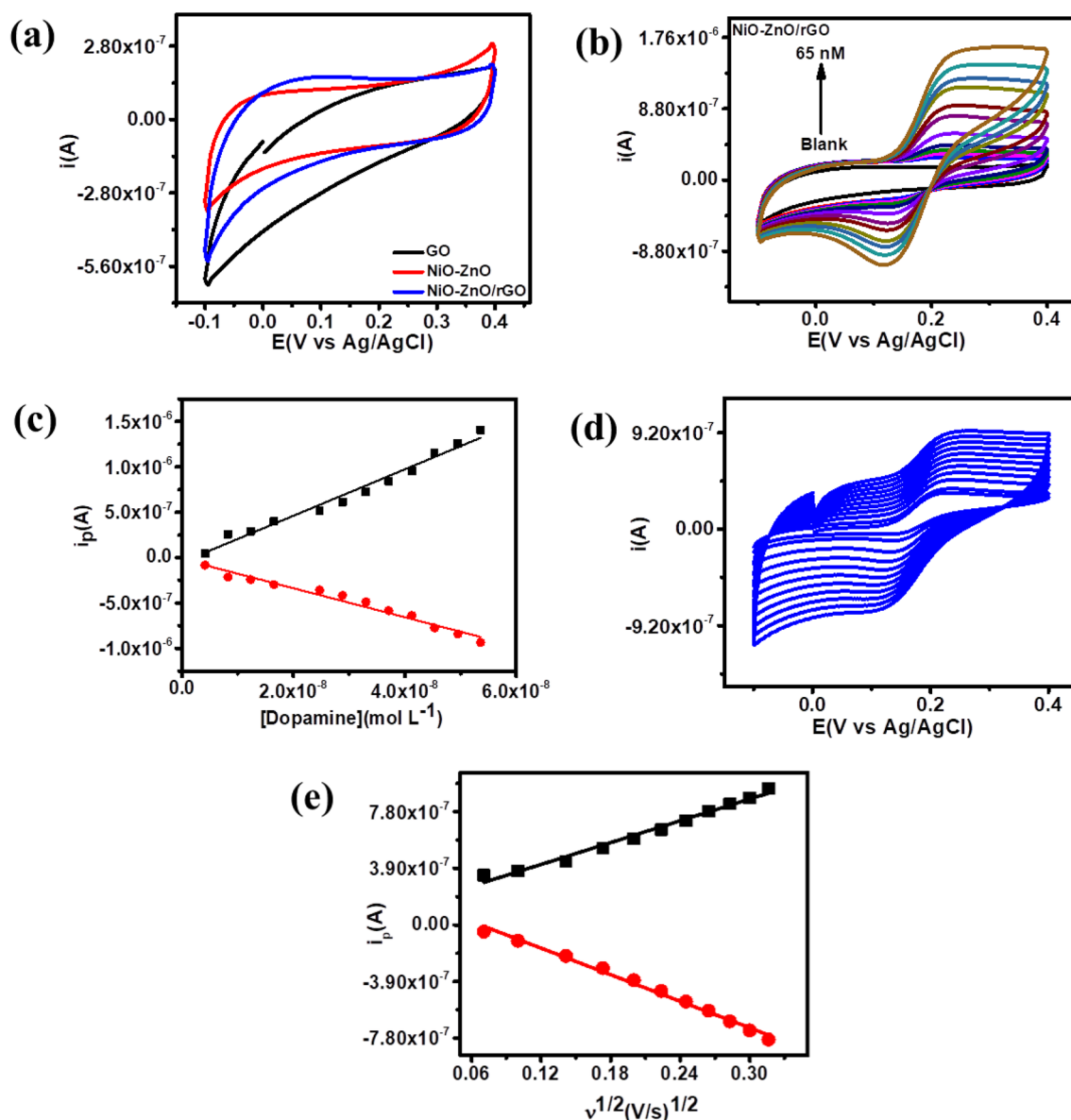


Fig. 5 **a** Blank Cyclic Voltammetry (CV) of rGO, NiO–ZnO, and NiO–ZnO/rGO-modified GCE in 0.1-M acetate buffer (pH 7.4). **b** Overlay CVs of NiO–ZnO/rGO-modified GCE with increasing concentration of DA. **c** The peak current versus

[DA]. **d** CV at different scan rates ranging between 10 and 100 mVs^{-1} . **e** Plot of the pulse peak current versus square root of scan rate

$$y = 2.06303 \times 10^{-7} - 3.05195 \times 10^{-6} (R^2 = 0.9915). \quad (3)$$

To investigate the effect of proton on the redox response of DA, the pH-dependent oxidation behavior of DA is investigated in different protonic media and is depicted in Fig. 6a. The study reveals that over a pH spectrum from acidic to basic (3.6–10), CV was used to investigate the redox activity of 28.8 nM DA at NiO–ZnO/rGO. At each pH level, the DA undergoes

a distinct oxidation reaction. Since DA exhibits a well-defined catalytic current reaction at pH 7.4, As pH increased, the oxidation peak potential of DA decreased, which a lower oxidation barrier in less protic environments.

Figure 6b illustrates the influence of pH on the peak current (I_{pa}) of 28.8-nM DA by modulating the pH (3.6–10) of the supporting electrolyte (0.1-M Acetate buffer system) at a scan rate of 50 mVs^{-1} . It was

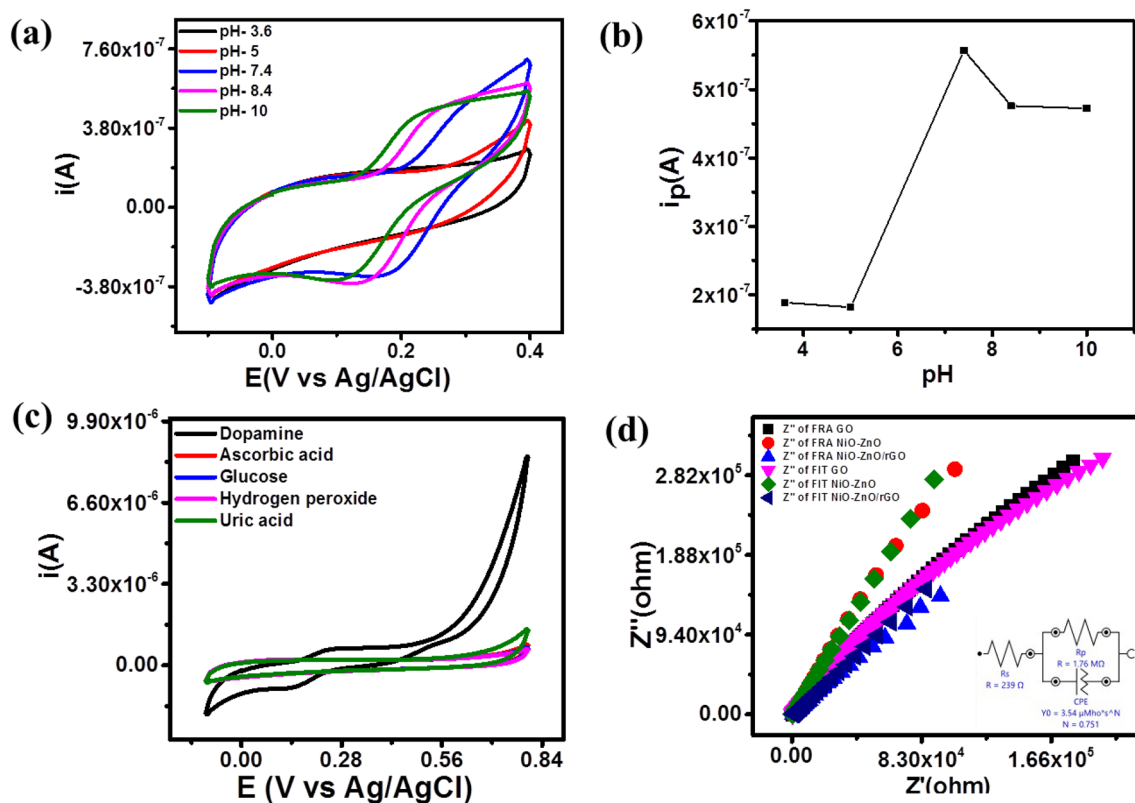


Fig. 6 CVs at the NiO–ZnO/rGO in 0.1-M acetate buffer, **a** DA with increasing pH (3–10). **b** Peak currents versus pH, **c** Selectivity study with 28.8-nM DA in the presence of 33 nM AA, Glu-

discovered that the maximum peak current of DA is produced at pH 7.4, which is close to the physiological pH (7.35 to 7.45).

3.6.1 Selectivity study

In the presence of large concentrations of physiologically active interfering substances, the selectivity of the NiO–ZnO/rGO sensor for the measurement of DA was tested. CVs of DA in the presence of interfering biomolecules glucose, Ascorbic acid, Uric acid, and hydrogen peroxide are depicted in Fig. 6c by performing a selectivity experiment. The presence of these molecules has no effect on the peak position or peak current of DA.

Figure 6d depicts the NiO–ZnO/rGO Nyquist plots. In the presence of 1 mM ferrocene, the faradic electrochemical impedance of modified electrodes is investigated. The impedance analysis revealed that the interfacial electron transfer is barrier free for the modified electrode because its value of charge transfer

resistance was 0.0162 ohm as opposed to 1.76 ohm for the bare electrode. AC amplitude of 10 mV is used to perturb the system with a predetermined frequency range of 10 kHz to 100 MHz. The semicircular portion on the side with the higher frequency controls the impedance to electron transfer between the electrode and electrolyte, thereby controlling the electron transfer rates for the redox sensor at the electrode interface. The linear part at low frequencies corresponds to the diffusion process between the electrode and electrolyte. Chronoamperograms ($i-t$ curve) of 28.8 nM of dopamine studied for NiO–ZnO/rGO nanocomposite exhibits the excellent deviation in the curve shown in Fig. 7a.

In Fig. 7b stability recorded after 100 cycles of CV and plot the graph percentage efficiency Vs number of CV cycle of NiO–ZnO/rGO nanocomposite. which shows 123% retention current of its initial current value after 100 cycle. This reveals that extreme stability of this sensor to DA.

Using Randles–Sevcik equation [42] sensitivity of composite can be calculated.

Using Randles–Sevcik equation [42] sensitivity of composite can be calculated.

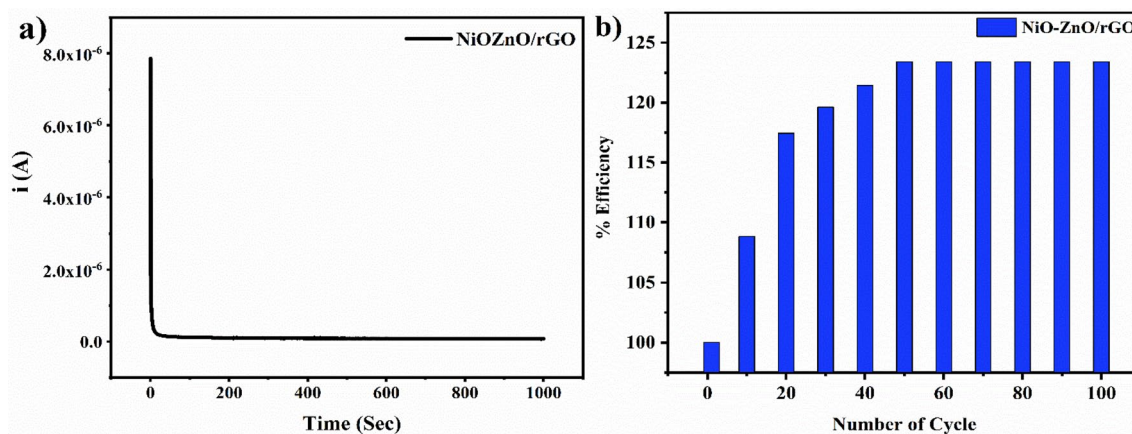


Fig. 7 **a** Chronoamperogram (i - t curve) of NiO-ZnO/rGO. **b** Plot of % efficiency Vs Number of CV cycle of NiO-ZnO/rGO nanocomposite

Table 2 Analysis of real samples of dopamine

Voluntary-1			Voluntary-2		
Added (nM)	Found (nM)	%Recovery	Added (nM)	Found (nM)	%Recovery
24.7	23.9	96.8	24.7	24	97.2
49.5	48.5	98	49.5	48.8	98.6

$$I_{pa} = 2.69 \times 10^2 n^3 D^{\frac{1}{2}} v^{\frac{1}{2}} AC \quad (4)$$

where $I_{p.a.}$ is the oxidation pulse peak current of DA; n is the total number of electrons transferred; and A is the electrochemically active surface area of the working electrode (cm^2). The sensitivity and LOD were calculated from the calibration plot and found to be $12.19 \mu\text{A L cm}^{-2} \text{Mol}^{-1}$ and LOD as low as $0.0076 \mu\text{M}$. The free energy of oxidation/reduction depends on the size and morphology of the electrocatalyst, orientation of solvent dipoles (water) and analyst (DA), and on the electrical-double layer at the surface of the electrode. Also we get oxygen depletion in nanocomposite which confirmed by EDS analysis, since we have obtained enhanced conductivity, sensitivity, and stability in the composite, we conclude that the sensor surface is barrier free for the oxidation of DA and hence, we get good redox response of DA.

3.7 Analysis of real samples of dopamine

The NiO-ZnO/rGO-modified electrode for the detection of DA in human urine samples was demonstrated. The recovery rate is 97.7% and the measurement

values of DA are very compatible with standard values. These findings, which are shown in Table 2, show that the NiO-ZnO/rGO has many potential uses for the accurate detection of DA in urine samples.

4 Conclusion

NiO-ZnO/rGO composite demonstrated to be a stable, selective, efficient and effective DA detector. From the spectral and morphological study we conclude, the Van der Waals interaction of the hexagonal shape of ZnO and the rods of NiO on a reduced graphene oxide sheet is first time reported. GCE modified with NiO-ZnO/rGO nanocomposites is used for electrochemical detection of DA. The redox response of the designed sensor found non-catalytic in high and less protic environment suggest the electron transfer process of DA at electrode surface is proton dependent. At a physiological pH of 7.4, the assay yields a significant response with a broad dynamic range of 0.0041 – $0.054 \mu\text{M}$, an active area of $2.1 \times 10^{-6} \text{cm}^2$, a high sensitivity of $12.19 \mu\text{A L cm}^{-2} \text{Mol}^{-1}$, and a LOD as low $0.0076 \mu\text{M}$. The observed LOD of our materials for DA is extremely low compared

Table 3 Comparisons of the electrochemical efficiency in the detection of DA between this research and earlier accounts

Electrode	Linear range (μM)	Detection limit (μM)	References
NiO/GO	2.0–60	0.100	[43]
ZnO/rGO	5.0–70	0.167	[44]
Ag–Cu-decorated/ ZnO	0.1–10	0.210	[45]
rGO_M	5–42	0.110	[46]
ZnO–rGO AuNPs	0.5–100	0.294	[47]
ZrO ₂ /ZnO	0.5–100	0.0094	[48]
ZnO@Au core shell	0.1–500	0.0086	[49]
CuO–NiO	1.0–6.0	0.033	[50]
NiO–ZnO/rGO	0.0041–0.054	0.00760	This work

to the literature cited in Table 3 itself indicates the trace detection ability of designed sensor. Decoration of rGO with NiO–ZnO can produce superior electrochemical substrates for DA analysis due to the increased active surface area and their unique interactions.

5 Limitations and anticipated forthcoming opportunity in NiO–ZnO/rGO nanocomposite

One significant limitation of hydrothermal synthesis is the inability to directly observe the crystal growth process in real time. The success of hydrothermal synthesis is highly dependent on the choice of solvent and its critical point properties. In our study, rGO provided a 2D platform for NiO and ZnO adsorption to enhance the surface-to-volume ratio. NiO and ZnO have high catalytic and electroactive properties. Based on the current experimental finding (the Van der Waals force), Drop casting is simplest and speedy technique of designing electrochemical sensor. it suggests wide scope in the following fields:

1. Photocatalyst for Organic Pollutants, Energy Storage (Supercapacitor, Battery and Solar Cell).
2. Hazardous gas sensing (ammonia, CO, NO_x, LPG).
3. HER and OER, pesticide detection, and other neurotransmitter detection, e.g., glucose.
4. Electrode material for non-invasive and wearable dopamine biosensors. The further improvement in

sensing can be done by studying the composition variation and loading of NPs optimization.

Author contributions

SNT conceptualized the synthesis method. GKC optimized and synthesized the NiO–ZnO/rGO composite materials under supervision of SNT and KVG. JVK, AAP and GKC characterized all the samples and also SSM and CKH characterized all the samples. AKT and GKC performed the electrochemical experiments in supervision of SNT and KKS. SNT supervised the overall research. All authors discussed and wrote the manuscript for final communication.

Funding

This research has not received any external funding.

Data availability

Data sharing is not applicable to this article as no datasets were generated or analyzed during the current study.

Declarations

Conflict of interest The authors declare that they have no known competing financial interests or personal relationships that could have appeared to influence the work reported in this paper.

References

1. P. Apelgren, M. Amoroso, K. Säljö, M. Montelius, A. Lindahl, L. Stridh Orrhult, P. Gatenholm, L. Kölby, S. Arulkumar, S. Parthiban, A. Goswami, R.S. Varma, M. Naushad, M.B. Gawande, J. Lipskas, K. Deep, W. Yao, S.P. Grogan, E.W. Dorthé, N.E. Glembotski, F. Gaul, D.D. D’Lima, E.E. Beketov, E.V. Isaeva, N.D. Yakovleva, G.A. Demyashkin, N.V. Arguchinskaya, A.A. Kisel, T.S. Lagoda, E.P. Malakhov, V.I. Kharlov, E.O. Osidak, S.P. Domogatsky, S.A. Ivanov, P.V. Shegay, A.D. Kaprin, Y. Sun, Q. Wu, Y. Zhang, K. Dai, Y. Wei, A. Dhawan, P.M. Kennedy, E.B.

- Rizk, I.T. Ozbolat, K. Ma, T. Zhao, L. Yang, P. Wang, J. Jin, H. Teng, D. Xia, L. Zhu, L. Li, Q. Jiang, X. Wang, C. Fiscale, R. Trattamento, T. Tel, R. Della, P. Dei, D.I. Adempiere, A.D. Un, O. Di, D.A. Salvatore, *Mater. Today Proc.* **27**, 1–31 (2019)
2. N. Pandech, T. Kongnok, N. Palakawong, S. Limpijumnong, W.R.L. Lambrecht, S. Jungthawan, *ACS Omega*. **5**, 25723 (2020)
3. S. Lakard, I.A. Pavel, B. Lakard, *Biosensors*. **11**, 179 (2021)
4. M.O. Klein, D.S. Battagello, A.R. Cardoso, D.N. Hauser, J.C. Bittencourt, R.G. Correa, *Cell. Mol. Neurobiol.* **39**, 31 (2019)
5. R.I. Teleanu, A.G. Niculescu, E. Roza, O. Vladăcenco, A.M. Grumezescu, D.M. Teleanu, *Int. J. Mol. Sci.* **23**, 5938 (2022)
6. C.H. Voon, K.L. Foo, B.Y. Lim, S.C.B. Gopinath, Y. Al-Douri, *Met. Oxide Powder Technol.* (2020). <https://doi.org/10.1016/B978-0-12-817505-7.00003-8>
7. M.C.B.S.M. Montenegro, *J. Pharm. Sci.* **89**, 876 (2000)
8. H. Zhao, H. Mu, Y. Bai, H. Yu, Y. Hu, *J. Pharm. Anal.* **1**, 208 (2011)
9. M. Tayyab, Y. Liu, Z. Liu, Z. Xu, W. Yue, L. Zhou, J. Lei, J. Zhang, *Chem. Eng. J.* **455**, 140601 (2023)
10. F. Bashar, K. Eddin, *Sensors*. **20**, 1 (2020)
11. A. Naharway, A. Hammad, A. bakr, A. Mansour, *Appl. Phys. A* **126**, 1–11 (2020)
12. M. Tayyab, Y. Liu, Z. Liu, L. Pan, Z. Xu, W. Yue, L. Zhou, J. Lei, J. Zhang, *J. Colloid Interface Sci.* **628**(B), 500–512 (2022)
13. Y.X. Gan, A.H. Jayatissa, Z. Yu, X. Chen, M. Li, *Nanomaterials* (2020). <https://doi.org/10.1155/2020/8917013>
14. A. Elzawy, A. Mansour, H. Magar, A. Hammad, R. Hassan, A. Nahrawy, *Materialstoday Commun.* **33**, 104574 (2022)
15. K. Dhara, R.M. Debiprosad, *Anal. Biochem.* **586**, 113415 (2019)
16. B. Rajeswari, K. Venkata, N. Suresh, *Biointerface Res. Appl. Chem.* **12**, 6058 (2022)
17. S.A. Khayyat, S.G. Ansari, A. Umar, *J. Nanosci. Nanotechnol.* **14**, 3569 (2014)
18. N.G. Mphuthi, A.S. Adekunle, O.E. Fayemi, L.O. Olasunkanmi, E.E. Ebenso, *Sci. Rep.* **7**, 1 (2017)
19. D. Balram, K.Y. Lian, N. Sebastian, *Int. J. Electrochem. Sci.* **13**, 1542 (2018)
20. O.E. Fayemi, A.S. Adekunle, *J. Biosens. Bioelectron.* (2015). <https://doi.org/10.4172/2155-6210.1000190>
21. N. Roy, S. Yasmin, S. Jeon, *Microchem. J.* **153**, 104501 (2020)
22. P.N. Manikandan, V. Dharuman, *Electroanalysis*. **29**, 1524 (2017)
23. A. Pandikumar, G.T. Soon How, T.P. See, F.S. Omar, S. Jayabal, K.Z. Kamali, N. Yusoff, A. Jamil, R. Ramaraj, S.A. John, H.N. Lim, N.M. Huang, *RSC Adv.* **4**, 63296 (2014)
24. H. hashtroudi, R. kumar, R. Savu, S. Moshkalev, G. Kawamura, A. Matsuda, M. Shafiei, *Int. J. Hydrog. Energy*. **46**, 7653–7665 (2021)
25. D. Rana, S. Kalia, R. Kumar, N. Thakur, D. Singh, R. Singh, *Mater. Chem Phys.* **287**, 126283 (2022)
26. D.C. Marcano, D.V. Kosynkin, J.M. Berlin, A. Sinitskii, Z. Sun, A. Slesarev, L.B. Alemany, W. Lu, J.M. Tour, *ACS Nano*. **4**, 4806 (2010)
27. A. Klechikov, J. Yu, D. Thomas, T. Sharifi, A.V. Talyzin, *Nanoscale*. **7**, 15374 (2015)
28. M.S.A. Faiz, C.A.C. Azurahaman, S.A. Raba, M.Z. Ruzniza, *Results Phys.* **16**, 102954 (2020)
29. H.A.S.Y. Lye, S.M.I. Asshari, B.Y.A. Manap, *J. Mater. Sci. Mater. Electron.* **29**, 9643 (2018)
30. R. Kumar, S.M. Yousrri, H.M. Soe, M.M. Abdel-Galeil, G. Kawamura, A. Matsuda, *J. Energy Storage*. **30**, 101539 (2020)
31. S.M. Yousrri, M.N. El-Nahass, R. Kumar, I.S. El-Hallag, W.K. Tan, A. Matusda, *J. Energy Storage*. **30**, 101485 (2020)
32. Z. Guo, G. wang, H. Fu, P. Wang, J. Liao, A. wang, *RSC Adv.* **10**, 26133 (2020)
33. X. Wang, L. Zhang, Z. Zhang, A. Yu, P. Wu, *Phys. Chem. Chem. Phys.* **18**, 3893 (2016)
34. N. Kaur, E. Comini, N. Poli, D. Zappa, G. Sberveglieri, *Procedia Eng.* **168**, 1140 (2016)
35. B.R.M. David, S. Hall, Lockwood, shawn poirier, christina bock. *J. Phys. Chem.* **116**, 6771 (2012)
36. A.M. Rao, J. Chen, E. Richter, U. Schlecht, P.C. Eklund, R.C. Haddon, U.D. Venkateswaran, Y.K. Kwon, D. Tománek, *Phys. Rev. Lett.* **86**, 3895 (2001)
37. P. Wang, D. Wang, M. Zhang, Y. Zhu, Y. Xu, X. Ma, X. Wang, *Sens. Actuators B Chem.* **230**, 477 (2016)
38. C.C. Li, Z.F. Du, L.M. Li, H.C. Yu, Q. Wan, T.H. Wang, *Appl. Phys. Lett.* **91**, 2005 (2007)
39. W. Huang, S. Ding, Y. Chen, W. Hao, X. Lai, J. Peng, J. Tu, Y. Cao, X. Li, *Sci. Rep.* **7**, 1 (2017)
40. Z. Qu, Y. Fu, B. Yu, P. Deng, L. Xing, X. Xue, *Sens. Actuators B Chem.* **222**, 78 (2016)
41. A.A. Mirza, G.M. Ali, I.O.P. Conf, *Ser. Mater. Sci. Eng.* **870**, 1 (2020)
42. Ş. Ulubay, Z. Dursun, *Talanta*. **80**, 1461 (2010)
43. J. Gao, P. He, T. Yang, L. Zhou, X. Wang, *J. Electroanal. Chem.* **852**, 113516 (2019)

44. M. Cao, L. Zheng, Y. Gu, Y. Wang, H. Zhang, X. Xu, *Microchem. J.* **159**, 105465 (2020)
45. S. Ponnada, D. Gorle, M. Kiai, S. Rajagopal, R. Sharma, *Mater. Adv.* **2**, 5986 (2021)
46. J. Gaidukevic, R. Aukstakojyte, J. BArauskas, G. Niaura, *Appl. Surf. Sci.* **592**, 153257 (2022)
47. M. Gu, H. Xiao, S. Wei, Z. Chen, L. Cao, *J. Electroanal. Chem.* **908**, 116117 (2022)
48. L. Chen, S. Tian, J. Zhang, H. Zhang, L. Sheng, X. Wang, J. Fan, *Res. Sq.* (2023). <https://doi.org/10.21203/rs.3.rs-3375395/v1>
49. T. Beatto, W. Gomes, A. Etchegaray, R. Gupta, R. Mendes, *RSC Adv.* **13**, 33424 (2023)
50. H. Sathisha, *Chem. Data Collect.* **48**, 101081 (2023)

Publisher's Note Springer Nature remains neutral with regard to jurisdictional claims in published maps and institutional affiliations.

Springer Nature or its licensor (e.g. a society or other partner) holds exclusive rights to this article under a publishing agreement with the author(s) or other rightsholder(s); author self-archiving of the accepted manuscript version of this article is solely governed by the terms of such publishing agreement and applicable law.